Nanoscale

ROYAL SOCIETY OF CHEMISTRY

PAPER

View Article Online
View Journal | View Issue

Cite this: *Nanoscale*, 2025, **17**, 16654

Experimental and first principle DFT comprehensions of metal and bimetal modified bismuth titanate for wastewater treatment and CO_2 hydrogenation

Isha Arora,[a] Seema Garg, *[a] Andras Sapi, [b] Mohit Yadav, [b] Zoltán Kónya, [b] Pravin Popinand Ingole, [c] Ajay,[c] Sumant Upadhyay [d] and Amrish Chandra [e,f]

Received 26th March 2025,
Accepted 18th June 2025

DOI: 10.1039/d5nr01250c

rsc.li/nanoscale

Incorporating copper (Cu) and silver (Ag) at the bismuth titanate (BT) surface was carried out *via* hydrolysis method followed by calcination at 700 °C. Modified BT further tested for the photodegradation of a recalcitrant pollutant Bisphenol-A (BPA), followed by the evaluation of photocatalytic hydrogenation of CO_2 for selective production of CO and CH_4. Photodegradation studies were remarkable in BT doped with both the metals (labelled "BTCA") as compared to pristine BT and mono metal modified BT with Cu and Ag. In case of photocatalytic CO_2 hydrogenation, BTCA analyte demonstrated a proximal increase in CO_2 conversion efficiency, which enhanced up to 39.1% as compared to monometallic doped and pristine BT. CO was the primary product of CO_2 reduction, while CH_4 was also produced to a lesser level. As CH_4 selectivity increased, surface normalised CO_2 conversion rates declined. This result was attributed to the difference in the number of electrons required to convert CO_2 to CO or CH_4. In our previous work of pristine BT, methane selectivity was only 0.1–0.2% of the overall CO_2 conversion. Hence, present findings are based on the modification of BT with copper and silver, for the evaluation of electron transfer and abundance for enhanced selectivity for CH_4.

1 Introduction

Recalcitrant organic contaminants such as Bisphenol A (BPA), methyl orange, Atrazine, Phenol, *etc*. have received a lot of attention in recent past decades due to their biomagnification, and high environmental exposure. Because of their widespread industrial and civilization use, these contaminants are abundant in aquatic ecosystems and have the ability to accumulate for extended periods of time without degrading in natural sunlight. As a result, effective removal of such hazardous compounds from contaminated water streams is critical for wastewater treatment and maintaining ecological equilibrium. In this context, traditional physicochemical procedures such as flocculation, adsorption, extraction, and reverse osmosis, among others, simply transfer organic pollutants from one phase to another without dissolving them. Furthermore, traditional biological approaches have encountered difficulties in the decomposition of pollutants due to their complex morphology, inadequate biodegradability, and high toxicity. Therefore, pollutant degradation requires an effective and efficient alternative advanced technique. Semiconductor-based photocatalysis, with its economic pathway and great efficacy in the destruction of harmful pollutants, has emerged as a promising approach for environmental remediation.[1–8] Additionally, economic expansion produces enhanced energy consumption, which leads to an increase in environmental contamination, as has been examined in recent years.

CO_2 emissions have increased by 1.9% each year during the last 30 years, owing to increased use of fossil fuels. The IPCC anticipated that CO_2 emissions would grow by 40–110% by 2030. In 2011, fossil fuels met 81% of energy demand, with renewables accounting for only 13%. In the future, the proportion of renewable energy sources should be enhanced. The solution to the problem of increasing energy consumption in connection with environmental hazards presents a challenge for the entire society. Photocatalytic CO_2 reduction is an inter-

[a]*Department of Chemistry, Amity Institute of Applied Sciences, Amity University, Sector-125, Noida 201313, Uttar Pradesh, India. E-mail: sgarg2@amity.edu*
[b]*Department of Applied and Environmental Chemistry, University of Szeged, 6720 Szeged, Rerrich Béla tér 1, Hungary*
[c]*Department of Chemistry, Indian Institute of Technology, Delhi Hauz Khas, New Delhi 110016, India*
[d]*Amity Institute of Nanotechnology, Amity University, Noida, Uttar Pradesh, 201313, India*
[e]*Lexgin IP LLP T21/1602, Paras Tierea, Sector 137, Noida 201301, Uttar Pradesh, India*
[f]*Sharda School of Pharmacy, Sharda University, Greater Noida, Uttar Pradesh 201310, India*

esting and environmentally acceptable approach for reducing CO_2 emissions in the atmosphere that uses sunlight as a source of radiation.[9–13]

Layered perovskite family of compounds "Bismuth titanate" with its diversified phases including sillenite $Bi_{12}TiO_{20}$, Aurivillius-type $Bi_4Ti_3O_{12}$, and pyrochlore $Bi_2Ti_2O_7$, have recently piqued the interest of researchers as a most promising and novel photocatalyst. The Aurivillus family of compounds, $Bi_4Ti_3O_{12}$, is made up of two $BiTiO_3$ unit cells with a pseudo perovskite structure and layers of $(Bi_2O_2)^{2+}$. This compound is employed in a range of applications, including ferroelectrics, piezoelectric transducers, electrocatalysts, and infrared reflective coatings.[14–24] If we compare Bismuth titanate structure with the conventionally used TiO_2 photocatalyst, their electronic structure in a valence band consists of hybrid orbitals of O 2p and Bi 6s, whereas TiO_2's valence band is entirely composed of O 2p orbitals. The presence of the well-dispersed Bi 6s orbital has been proven to reduce the band gap as well as the recombination among the photogenerated charge carriers.[25] Moreover, modifying the desired catalyst has remarkable changes in terms of reducing recombination among photogenerated charge carriers, increasing surface area, enhancing selectivity of C1 products and promoting electron production.

Copper oxides are p-type semiconductors with narrow bandgaps (CuO, E_g = 1.35 to 1.7 eV; Cu_2O, E_g = 1.9 to 2.2 eV). Thus, it may be capitalised for photo-reduction of CO_2, but the VB of Cu_2O is considered insufficiently positive to oxidise the water (0.81 eV at pH = 7.0). Therefore, it cannot direct H_2O oxidation to OH radicals (2.3 eV *vs.* NHE). Due to its high VB oxidation potential, it is typically utilised in combination with other metal oxides rather than alone as a photocatalyst.[26,27] Furthermore, if we talk about modifying the semiconductor's properties, silver has also proven to be an exceptional metal. Silver nanoparticles have been shown to be the best sensing materials due to their various advantages, which include strong electron exchange ability, low cost, non-toxicity, and excellent chemical stability.[28,29] Hence, present work is focussed on robust synthesis of mono metal and bimetal doped Bismuth Titanate (BT) analytes for efficient photodegradation and enhanced photocatalytic CO_2 hydrogenation.

2 Experimental

2.1 Materials

All the analytical grade chemicals used for the fabrication of doped bismuth titanate (BT) includes Bismuth(III) nitrate pentahydrate ($Bi(NO_3)_3{\cdot}5H_2O$) obtained from merck, Titanium tetraisopropoxide ($Ti\{OCH(CH_3)_2\}_4$) obtained from Spectrochem Pvt. Ltd, Glacial acetic acid (CH_3COOH) obtained from Sisco Research Laboratories Pvt. Ltd, sodium hydroxide (NaOH) obtained from central drug house (CDH), Copper(II) nitrate pentahydrate ($Cu(NO_3)_2{\cdot}5H_2O$), silver nitrate ($AgNO_3$) from Merck, quercetin dihydrate, acetone (C_3H_6O) from Merck, ethanol (C_2H_5OH, extra pure for research analysis), obtained from Merck, all were used. For the study of photocatalytic CO_2 hydrogenation, highly pure gases were purchased.

2.2 Photocatalyst synthesis

2.2.1 Metal doped bismuth titanate. The synthesis of metal modified BT photocatalyst was carried out by hydrolysis method [Fig. 1(A and B)]. Equimolar solutions of Bismuth nitrate (BN) and Titanium isopropoxide (TTIP) were prepared. Afterwards, concentration studies for dopant metal based samples labelled as BT-Cu1 (0.1 mol% Cu), BT-Cu2 (0.2 mol% Cu), BT-Ag1 (0.001 M), BT-Ag2 (0.002 M Ag), was carried out. For the preparation of BT-Cu1 and BT-Cu2, amount of copper nitrate pentahydrate was first dissolved in 1 mL of ethanol, afterwards it was added in as prepared BN solution. Subsequently, 0.05 M of TTIP solution was added into above prepared solution under magnetic stirring followed by formulating a pH of 3. The resulting solution was stirred continuously before being placed in an oven at 60 °C for 1 h. After this, the sample was filtered, washed, and dried at 60 °C. Finally, the sample underwent calcination at 700 °C for 3 hours to obtain the desired material. Furthermore, BT-Ag1 and BT-Ag2 was prepared *via* a photoreduction approach. 500 mg of as-synthesised pure BT was disseminated in 30 mL quercetin solution. The clear suspension was then mixed with 100 mL of $AgNO_3$ solution and agitated for 1 h in the dark. The resulting slurry was then vigorously stirred and exposed to a 40 W UV lamp for 3 h following the photoreduction method to accumulate the Ag nanoparticles over the interface of BT. Finally, the silver modified BT samples after maintaining a pH of 3, were filtered, washed, and dried at 60 °C overnight. Then the dried BT-Ag1 and BT-Ag2 was calcined at 700 °C for 3 h.

2.2.2 Bimetal doped bismuth titanate. Similarly, to formulate bimetallic doped BT, copper (0.2 mol% Cu) and Silver (0.002 M Ag), both were utilised (Fig. 1C). For the synthesis, first BT-Ag was prepared *via* a photoreduction approach. 500 mg of as synthesised pristine BT was disseminated in 30 mL quercetin solution. The clean BT suspension was then mixed with 100 mL of $AgNO_3$ solution at a molar concentration of 0.002 M and agitated for 1 h in the dark, in this stage, 0.2 mol% of copper nitrate pentahydrate slurry was added in the suspension. The resulting slurry was then vigorously stirred and exposed to a 40 W UV lamp for 3 h. Finally, the as fabricated precipitate after maintaining a pH of 3, was filtered, washed, and dried at 60 °C overnight. After successful fabrication of bimetallic doped bismuth titanate, the nanocrystals were then calcined at 700 °C for 3 h. The as fabricated bimetallic photocatalyst was finally labelled as BTCA.

2.3 Characterization techniques

X-ray diffraction (XRD) patterns were obtained using a Siemens D5005 diffractometer with Cu Kα radiation. The surface structure of the analytes was examined using scanning electron microscopy (SEM). SEM images were captured with a Hitachi S-4700 scanning electron microscope, using an accelerating voltage between 10 and 18 kV. A FEI TECNAI G2 20 X-Twin high-resolution TEM was employed to further examine

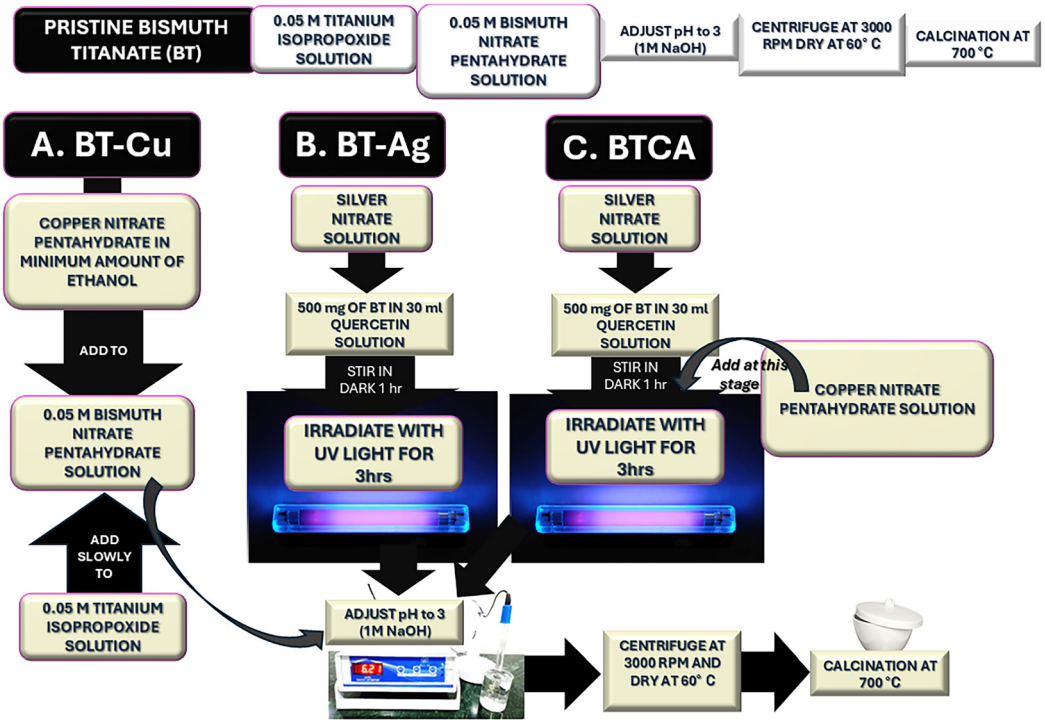

Fig. 1 Flow diagram for synthesis of metal modified BT (A: BT-Cu, B: BT-Ag) and bimetal modified BT (C: BTCA).

the morphology of the samples, and selected area diffraction (SAED) was utilized to collect data regarding the crystal structures. The specific surface area of the samples was measured using the Brunauer–Emmett–Teller (BET) method, which involved nitrogen adsorption at 77 K, with a Quantachrome NOVA3000 instrument. Prior to measurement, the sample surfaces were cleaned by flushing with N2 at 373 K for 5 h. The band gap energy (E_g, eV) of the as fabricated photocatalyst was determined from absorption measurements (λ, nm) obtained *via* UV-Vis spectrophotometry with diffuse reflectance. X-ray photoelectron (XP) spectra were acquired using a non-monochromatized Mg Kα X-ray source (1253.6 eV). The X-ray gun was operated at 144 W (12 kV, 12 mA) to obtain both survey and high-resolution spectra. Survey spectra were recorded with a pass energy of 80 eV and a step size of 1 eV. High-resolution spectra were recorded with a pass energy of 40 eV and an energy resolution of 0.1 eV. All high-resolution spectra were charge-corrected by referencing the aliphatic component of the C 1s spectrum to 284.8 eV. A Shirley background correction was applied to all spectra. Raman spectra were obtained using a Thermo Scientific™ DXR™ Raman microscope with a 635 nm excitation wavelength. The laser power was set to 10 mW, and 20 spectra were averaged with an exposure time of 6 seconds. A **Bruker Invenio-R FTIR** spectrometer with a Harrick Praying Mantis™ diffuse reflectance attachment was employed for diffuse infrared reflectance Fourier transform spectroscopy (DRIFTS). Two **ZnSe** windows were located in the infrared path of the sample holder. The samples were pretreated as detailed in section 2.5. After cooling to ambient temperature under helium flow, the background spectrum was recorded. At room temperature, a $CO_2 : H_2$ combination (1 : 2) with a total flow rate of 50 mL min^{-1} was supplied into the DRIFTS cell, followed by UV irradiation for 10 and 20 minutes. To prevent condensation, the tubes were heated externally. All spectra were obtained between 4000 and 900 cm^{-1} with a resolution of 2 cm^{-1}.

2.4 Photocatalytic degradation evaluation

The wastewater potential of the pristine, mono metal, and bimetal modified BT analytes was analysed *via* photocatalytic degradation of Bisphenol-A (BPA). The evaluation of BPA photodegradation of our as synthesised analytes was done using a UV-visible spectrophotometer. The experimental framework was visible light reactor with the four compact fluorescent bulbs of 28 W energy. Typically, set of experiments to analyse the photocatalytic efficacy of all the samples were performed individually where the optimised amount of catalyst was added to 100 ml stock solution of Bisphenol-A (BPA) stock solution of 20 mg L^{-1}. At first, for acquiring sufficient adsorption–desorption equilibrium in between the interaction of BPA on to the surface of modified BT photocatalyst, the solution was stirred in the dark for 60 min before being exposed to visible light lamps. At this stage the contaminated BPA/photocatalyst solution final pH was noted. Afterwards, the solution was then subjected to visible light irradiation while being continuously stirred. At predetermined intervals, 3 mL of the mixture was eliminated from the beaker and the absorbance value was noted in UV-vis spectrophotometer at 273 nm.

The experimental data for photo disintegration of BPA was calculated using the following equation (eqn (1)).

$$\text{Degradation } \% = \left[\frac{C_0 - C_t}{C_0}\right] \times 100 \quad (1)$$

where C_0 and C_t are the concentrations at the start (0) and time (t) correspondingly.

The rate constant for the adsorption of BPA dye molecules can be examined from the first-order kinetics equation (see eqn (2)):

$$-\ln\left(\frac{C_t}{C_0}\right) = -kt \quad (2)$$

where C_0 is the initial concentration and C_t is the concentration after the time (t). k is the apparent first-order rate constant given by the slope of the graph of $\ln C_0/C_t$ *versus* t.

2.4.1 Recyclability studies. Three successive cycles of reusability testing of the as optimised BTCA for BPA photodegradation under visible light were carried out. The samples were centrifuged at 3000 rpm and washed with distilled water then dried after each run. The photocatalytic efficacy of the catalyst was enumerated after each cycle.

2.4.2 Scavenging evaluation. The radical trapping evaluation was conducted to administer the active radical species responsible for photocatalytic efficacy, in which 1 mM solutions of sodium oxalate, isopropanol, and benzoquinone were used independently with the same photocatalytic technique as previously described. The role of active radical species (h^+, $^{\bullet}OH$, O_2^{-}) can be studied from this technique to successfully represent the correct photocatalytic mechanism. As optimised BTCA analysed was tested for confirming the role of active radical species in the degradation of BPA.

2.5 Photocatalytic CO_2 hydrogenation test

Photocatalytic CO_2 reduction analysis was carried out in a batch reactor with an inner glass (quartz) cylinder (h = 25 cm, diameter = 6.4 cm) and an outer glass (quartz) cylinder (h = 25 cm, diameter: 10.2 cm). The light source was a 500 W mercury vapour lamp (Heraeus Noblelight TQ 718, Hanau, Germany; λ_{max} = 254 nm). A Quantum meter (Apogee, Model MQ-200) was used to evaluate the irradiation intensity of the lamps on the photocatalytic surface. Pre-treatment of the sample includes ultrasonic dispersion of 200 mg of catalystin 10 mL of 100% ethanol, then it was immobilised on the outer surface of the inner quartz cylinder. The prepared catalyst film was then processed with a heating rod at 250 °C with the introduction of various gases (Ar for 20 min, O_2 for 30 min, Ar for 10 min, and H_2 for 60 min) into the gap between the cylinders. The reactant gas mixture, $CO_2 : H_2$, was then purged into the reactor using a mass flow controller (Aalborg). A pump was used to circulate a set volume of reactant gas mixture between the reactor and the gas chromatograph (GC). During the measurements, cooling water was recirculated to keep the system at a consistent temperature. The products and reactants were identified and separated using an HP 5890 Series II GC with a packed Porapak QS column (0.635 cm diameter, 2 m length). The resultant compounds were detected using a thermal conductivity detector and a flame ionisation detector.

The conversion of CO_2 and the selectivity of various components (CO, CH_4,) in the product stream were calculated using specific equations, were calculated using the following eqn (3) and (4) below:[30]

$$\text{Conversion } \%, X_{CO_2} = \left[\frac{\text{moles of } CO_2\text{(inlet)} - \text{moles of } CO_2\text{(outlet)}}{\text{moles of } CO_2\text{(inlet)}}\right] \times 100 \quad (3)$$

$$\text{Selectivity}_{\text{product}} \% = \left[\frac{\text{moles of product}}{\text{total moles of products}}\right] \times 100 \text{ (carbon atom basis)} \quad (4)$$

2.6 Photoelectrochemical measurements

Photoelectrochemical (PEC) measurements were carried out using a CHI 604E potentiostat coupled with a 150 W Xe arc lamp as the light source. A standard three-electrode configuration was used, comprising a platinum wire as the counter electrode, a saturated Ag/AgCl/Cl^- electrode as the reference, and a working electrode made from an FTO glass substrate coated with catalyst ink. The electrolyte solution for PEC analysis consisted of 1 M Na_2SO_4 with 5% H_2O_2. To prepare the working electrode, 2 mg of the catalyst was dispersed in a mixture of 10 μL Nafion, 50 μL ethanol, and 50 μL water, then ultrasonicated. A 10 μL portion of this suspension was drop-cast onto an FTO-coated glass slide with a surface area of 1 cm^2. Transient photocurrent response measurements were performed at −0.3 V *versus* the Ag/AgCl/Cl^- reference electrode. Additionally, electrochemical impedance spectroscopy (EIS) was conducted at the same potential over a frequency range of 1 Hz to 10 MHz.

3 Results and discussion

3.1 Structural analysis

3.1.1 XRD. XRD results of pristine and modified BT are depicted in Fig. 2. In pristine BT, we could observe a very sharp intensity at 30° with (1 17) plane which is the characteristic peak of $Bi_4Ti_3O_{12}$, several other low yet sharp intense peaks depict the presence of $Bi_{12}TiO_{20}$ and $Bi_2Ti_2O_7$ phases as well. In modified BT with optimised amount of copper and silver (BT-Cu2, BT-Ag2) and both the metals (BTCA), we could observe a prominent arrival of few additional peaks which were represented as the characteristic peaks of silver and copper. In BT-Cu2, a prominent peak of copper oxide (CuO) appeared at 2θ = 38.7°, which was attributed to the preferred orientation crystal plane of (111) and was consistent with CuO nanoparticle phase (JCPDS card no. 48-1548)[27] was observed. Moreover, in BT-Ag2 analyte, one characteristic peak of Ag nanoparticle was observed at 2θ = 38.10° which was attributed to the crystal plane of (111) of Ag nanoparticle and was consistent with JCPDS file no. 04-0783.[29] In bimetallic modified

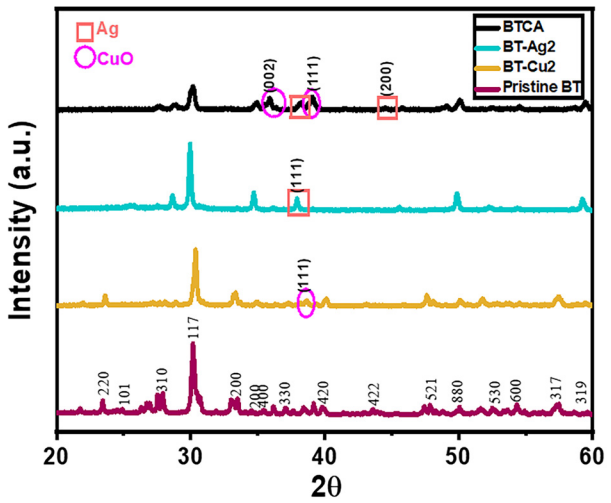

Fig. 2 XRD patterns of Pristine BT, BT-Cu2, BT-Ag2, BTCA.

bismuth titanate 'BTCA', characteristic peaks of CuO and Ag were seen at 2θ = 35.5°, and 44.3° respectively, well matched with the literature.[27,29] Also, one prominent peak of Ag nanoparticle at 2θ = 35.5° was in alignment with the characteristic peak of CuO at 2θ = 38.1°, both acquiring crystal plane of (111), proving that both metals have been successfully incorporated into the crystal lattice of Bismuth titanate. Successful incorporation of metals has been proved with the XRD peaks. However, as we move from pristine BT to bimetallic modified BT (BTCA), we could observe that a very sharp intensity peak at 30° with (117) plane became less intense and the intensity of a peak at 50° with (8 8 0) plane became sharp which could imply that the alteration using both the metals favours the formation of crystallographic plane of polychlore "$Bi_2Ti_2O_7$" and successful incorporation of both the metals into this plane of BT, which is further demonstrated with first principle DFT analysis.

The average crystallite size and interplanar *d*-spacing is calculated using the Scherrer equation and bragg's equation (eqn (5) and (6)).

$$D = 0.9\lambda/(\beta \cos \theta) \quad (5)$$

$$d = \frac{n\lambda}{2 \sin \theta} \quad (6)$$

The average crystallite size was estimated using the position of the indexed high intensity peaks in the XRD pattern as well as their FWHM values. The average crystallite size, specific surface area, interplanar *d*-spacing and average particle size for Pristine BT, BT-Cu2, BT-Ag2 and BTCA is shown in Table 1.

3.1.2 XPS. The chemical composition and elemental oxidation state of modified BT analytes were determined using XPS [Fig. 3(a–j)]. Bi 4f, CuO, Cu 2p and Bi 4s high resolution scan for BT-Cu2 is depicted in Fig. 3(b and c); Bi 4f, Ag 3d for BT-Ag2 is depicted in Fig. 3(e and f), High resolution scan of Bi 4f, CuO, Bi 4s, Ag 3d for BTCA is given in Fig. 3(h–j); finally, high resolution scan of Ti 2p and Bi 4d, C 1s, and O1s is given in Fig. 3(k–m). Moreover, survey scan spectra of BT-Cu2, BT-Ag2, and BTCA are given in Fig. 3(a, d and g) respectively. All scans indicated that the analytes possess their own constituent elements (Bi 4f, Bi 4d, Ti 2p, Cu 2p, Bi 4s, Ag 3d), and C 1s and O1s arose due to the analytes' contact with air. XPS revealed the existence of metals, and the distinctive spectra of Cu 2p and Ag 3d nanoparticles corresponded to the results of XRD examination of BT-Cu2, BT-Ag2, and BTCA analytes. Fig. 3(k) shows the Bi 4d and Ti 2p XPS spectra of the nano powder which reflected 3/2 component of Bi(III), as well as 1/2 and 3/2 component of Ti(IV), which clearly represents Bi in +3 oxidation state and Ti in +4 oxidation state. The Bi 4f fine doublet spectra of the analyte under study are shown in Fig. 3 (b and e) for **BT-Cu2, and BT-Ag2**, which depicts two sharp peaks at 158.9 and 164.2 eV which are the binding energies of Bi 4f (5/2) and Bi 4f (7/2). Whereas in case of BTCA, peaks range was shifted to lower levels depicting two peaks at 158.7 and 164.1 corresponding to binding energies of Bi 4f (5/2) and Bi 4f (7/2). This shift towards lower binding energy can be attributed to a change in local chemical environment of bismuth atoms, which is most likely caused by synergistic electronic interactions between co-incorporation of copper and silver. These interactions may cause a minor increase in electron density around the Bi atoms, lowering the effective nuclear charge experienced by the core electrons and therefore decreasing the binding energy. Such alterations are indicative of successful co-doping and point to an altered electronic structure in the BTCA sample. The Bi 4f and Ti 2p peaks are well matched with the pure Bi_2O_3 and TiO_2, which are intermediates formed during the hydrolysis of bismuth nitrate and titanium isopropoxide separately. C 1s Spectra in Fig. 3(l) reflected peaks, which were attributed to aliphatic carbons (C–C, C–H), alcoholic and carbonyl functional group (C–OH and

Table 1 Depicting specific surface area, pore size distribution, average crystallite size, interplanar *d*-spacing, band gap and average particle size of Pristine BT, BT-Cu2, BT-Ag2, and BTCA

Sample name	Specific surface area ($m^2\ g^{-1}$)	Total pore volume ($cc\ g^{-1}$)	Average pore diameter (nm)	Average crystallite size (nm)	Average interplanar spacing (*d*-spacing) in Å	Band gap (eV)	Average particle size (nm)
Pristine BT	5.5	0.008904	6.43359	21.6	—	2.82	82
BT-Cu2	8.9	0.01455	8.09809	23.5	2.3	2.70	92
BT-Ag2	6.9	0.01185	10.5968	33.9	2.4	2.74	124
BTCA	4.1	0.00914	8.84376	19.0	2.3	2.66	129

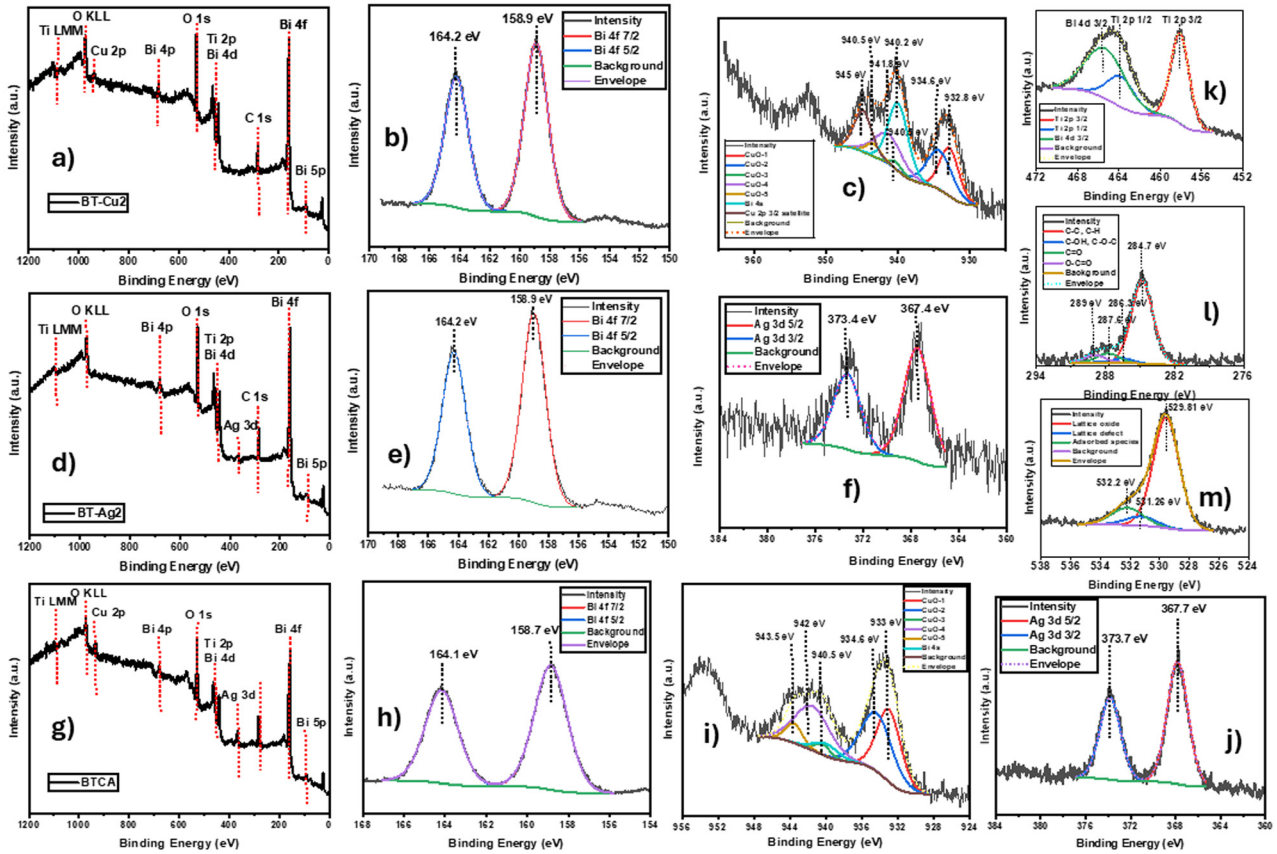

Fig. 3 X-ray photoelectron spectroscopy of BT-Cu2, BT-Ag2, and BTCA; high resolution scan of BT-Cu2 (b) Bi 4f, (c) CuO, Cu 2p and Bi 4s; high resolution scan of BT-Ag2 (e) Bi 4f, (f) Ag 3d; high resolution scan of BTCA (h) Bi 4f, (i) CuO and Bi 4s, (j) Ag 3d; high resolution scan of (k) Ti 2p and Bi 4d, (l) C 1s, (m) O1s; survey scan spectra of (a) BT-Cu2 (d) BT-Ag2 (g) BTCA.

C–O–C), sp2 hybridised carbons (aromatic rings, C═O), and carbonyl functional group (O–C═O). The high resolution spectra of O 1s in Fig. 3(m) showcased peak at 529.81 eV, corresponding to oxygen bonded with Bi(III) ions (Bi_2O_3), another peak at 531.26 eV is due to the presence of oxygen vacancy in the lattice, and a peak at 532.2 eV is due to the presence of moisture and adsorbed organic species in pristine bismuth titanate calcined analyte. In Fig. 3(f), the binding energy of the Ag 3d 5/2 peak is 367.4 eV for BT-Ag2 and in BTCA its value for binding energy increase to 367.7 eV. Based on the binding energy values the Ag must be in oxide form, but XRD and synthesis method confirms its presence in Ag metallic for which is acting as an electron sink for enhancing photocatalytic efficacy. The shift in the binding energy suggests that the Ag could be partially oxidized or in a mixed valence state. In Fig. 3(c and i), the copper detected is CuO, and its signal is fit with the peak structure described in the literature.[27] However, in Fig. 3(c), one peak exhibits an additional Cu 2p satellite peak at binding energy of 945 eV. Furthermore, the Cu 2p region strongly overlaps with the 4s transition of the Bi, proposing the fact that it strongly bounded with the lattice of BT. Binding energy value for CuO also increase for BTCA as compared to BT-Cu2. The copper in BTCA may experience stronger electron-withdrawing interactions from the BT matrix, causing an increase in the oxidation state of Cu and, in turn, an increase in its binding energy.

3.1.3 Textural analysis. The as-synthesised and optimised pristine BT, BT-Cu2, BT-Ag2, and BTCA analytes were inspected by the N_2 adsorption–desorption method to assess the specific surface area. The as-prepared Pristine BT, BT-Cu2, and BT-Ag2 samples promoted a Type III isotherms, following the fact that BT-Ag2 have a slight hysteresis among the adsorption and desorption curves, as compared to Pristine BT, and BT-Cu2. Furthermore, BTCA represented Type IV with H4 hysteresis loop, which is in accordance with the IUPAC classification [Fig. 4(b–e)]. The presence of large hysteresis among the adsorption and desorption curves in BTCA, depicts the presence of mesoporous structure (Fig. 4e). The specific surface area of BTCA was found to be 4.1 $m^2\ g^{-1}$ respectively. The higher surface area would provide a large contact area for the reactant molecules to approach the photoactive sites for the maximum adsorption. As it was obtained that BTCA possessed surface area less than the mono metal modified BT, but a notable enhancement in photocatalytic efficiency, this decrease in surface area could be due to the formation of new crystallographic plane of BT in BTCA which was confirmed *via*

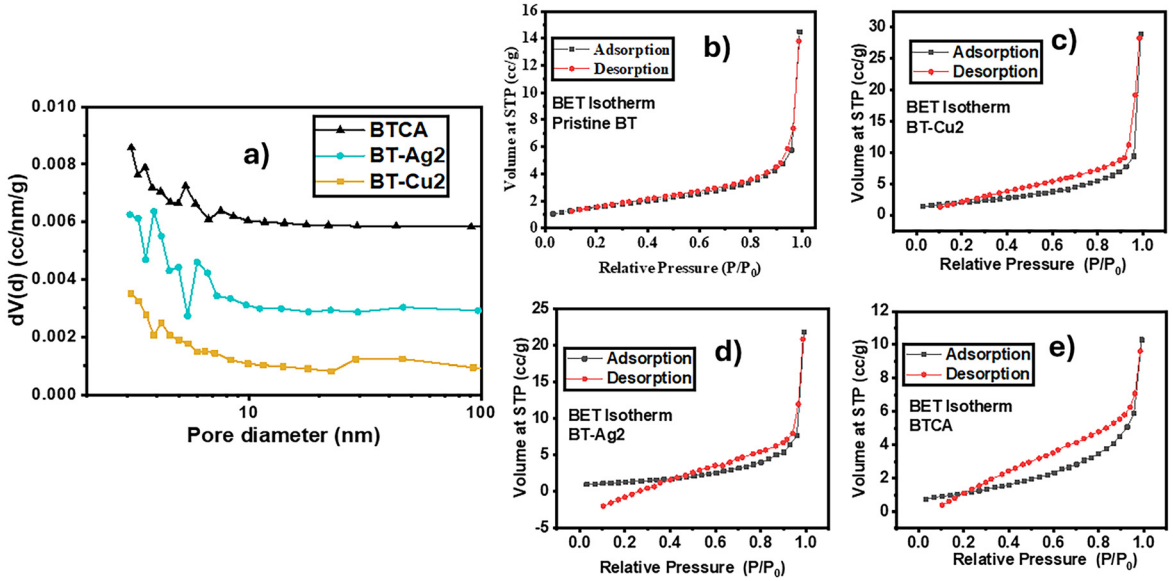

Fig. 4 (a) Pore size distribution of BT-Cu2, BT-Ag2, BTCA; (b–e) N2 adsorption desorption isotherm BT-Cu2, BT-Ag2, BTCA, Pristine BT.

XRD analysis. BT-Cu2 sample demonstrated narrow pore size distribution with a single peak in the 4.2 nm (Fig. 4a) implying a less porous material while BT-Ag2 sample exhibited peaks at 3.9 and 5.9 nm and BTCA exhibited peaks at 3.5, 5.4 and 7.2 nm implying a highly mesoporous structure.[31] However, according to PEC analysis, BTCA possessed least recombination centres for electrons and holes, hence, vigorous production and mobility of charge carriers in BTCA interface due to the addition of copper and silver promotes higher degradation efficacy under visible light irradiation as well as highest CO_2 adsorption.

3.1.4 Raman analysis. Raman analysis was carried out for further enumeration of the oxygen vacancies in interfacial crystal lattice of pristine and optimised modified bismuth titanate samples [Fig. 5(b)]. In pristine BT, the Raman shift in the frequency range 50–150 cm^{-1} correspond to Bi vibrations with regard to the oxygen octahedron, where particularly the shift at 63 cm^{-1} belongs to the so-called hard layer mode, which corresponds to the motion of the $(Bi_2O_2)^{2+}$ with respect to the oxygen octahedron. The weak shifts in the frequency range 200–400 cm^{-1} correspond to bending vibrations of the O–Ti–O bonds, while the high frequency lines in the range 500–650 cm^{-1} relate to stretching vibrations.[18] Furthermore, the optical characteristics of CuO nanoparticles in the BT-Cu2 analyte were further investigated in the Raman spectra of BT-Cu2. The peak at 258 cm^{-1} is allocated to the A_g mode, whereas the peak at 305 cm^{-1} are assigned to the B_g mode. The detected Raman peaks are compatible with the reported CuO nanostructures.[32] In case of BTCA, the peak at 258 cm^{-1} corresponding to the A_g mode of CuO displaying a wide shift.

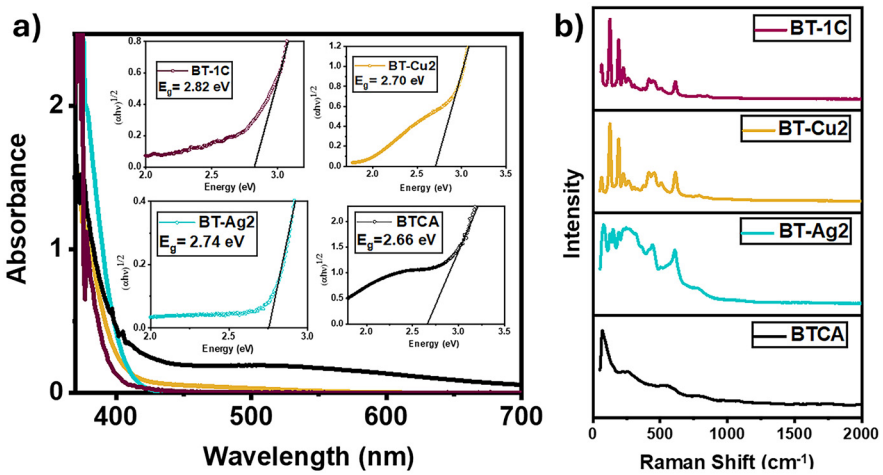

Fig. 5 (a) UV-DRS; and (b) Raman analysis of Pristine BT, BT-Cu2, BT-Ag2, and BTCA.

The E_g bands at 142 cm^{-1} and 196 cm^{-1} has a significant Raman frequency shift and increased half width, whereas the A_{1g}/B_{1g} band at 513 cm^{-1} has a mild frequency shift. Multiphonon scattering produces a broad complex band ranging from 220–300 cm^{-1}. Furthermore, in the Raman spectra of BT-Cu2, BT-Ag2, and BTCA analytes, the silver/copper atoms affect the local coordination of oxygen around Ti^{4+}, hence maintaining charge neutrality and creating oxygen vacancies in the bismuth titanium oxide lattice.[33]

3.1.5 Band gap analysis. The band gap analysis of as synthesised and optimised pristine, mono metal and bimetal modified BT analytes were recorded *via* UV-Vis DRS spectrophotometer in the range of 200–800 nm [Fig. 5(a)]. Therefore, an indirect band gap of metal and bimetal doped analytes was calculated *via* Tauc plot using the eqn (7), and it was showing a prominent decrease in the band gap of all modified samples as compared to Pristine BT which demonstrated a band gap of 2.82.

$$\alpha h\nu^{0.5} \rightarrow A(h\nu - E_g) \quad (7)$$

where, α = absorption coefficient, h = Planck's constant, ν = photon's constant, A = proportionality constant, E_g = band gap energy, n = nature of electronic transition.

Bimetallic doped bismuth titanate 'BTCA' demonstrated the least band gap energy value of 2.36 eV which is in accordance with its highest efficacy in dye degradation and CO_2 conversion percentage. Metal incorporation, on the other hand, may produce a redshift of the absorption edge due to the intermixing of Cu 2p, and Ag 3d orbitals with O 2p orbitals in the valence band of BT, resulting in a smaller bandgap energy among the mono metal doped BT analytes (BT-Cu2 and BT-Ag2). The observations are in alignment with the PEC measurements, degradation results and CO_2 hydrogenation analysis.

3.1.6 Computational details. All the first-principles density functional theory (DFT) based calculations were carried out as implemented in QuantumATK [AtomistixTool, Quantum ATK A., and S. Version "3 (2019) **https://www.quantumatk.com**" accessed Nov. (2018)]. Exchange–correlation interactions were described through generalized gradient approximation (GGA), within the Perdew–Burke–Ernzerhof (PBE) formulation.[34,35] Structural data for the stoichiometric $Bi_2Ti_2O_7$ pyrochlore ($Fd\bar{3}m$ space group no. 227) were chosen to build the initial configuration. A supercell of 2 × 2 × 2 was constructed from its optimized bulk unit cell having 88 atoms (Fig. 6a). To simulate the structure close to experimental values, one Ti atom was replaced with Cu (Fig. 6b) and Ag (Fig. 6c) and two atoms of Ti with both Cu & Ag atoms (Fig. 6d) supercell amounting to 6.25 atom% (for Cu & Ag) and 12.50 atom% for co-doped system. The electronic optimization and structural relaxation were performed until energy and forces converged to 10^{-4} eV and 0.02 eV $Å^{-1}$ respectively. The calculations of the total and partial density of states, and the band-structure were performed after geometric optimization. The Brillouin zone was sampled using 4 × 4 × 4 k-points generated using Monkhorst–Pack scheme

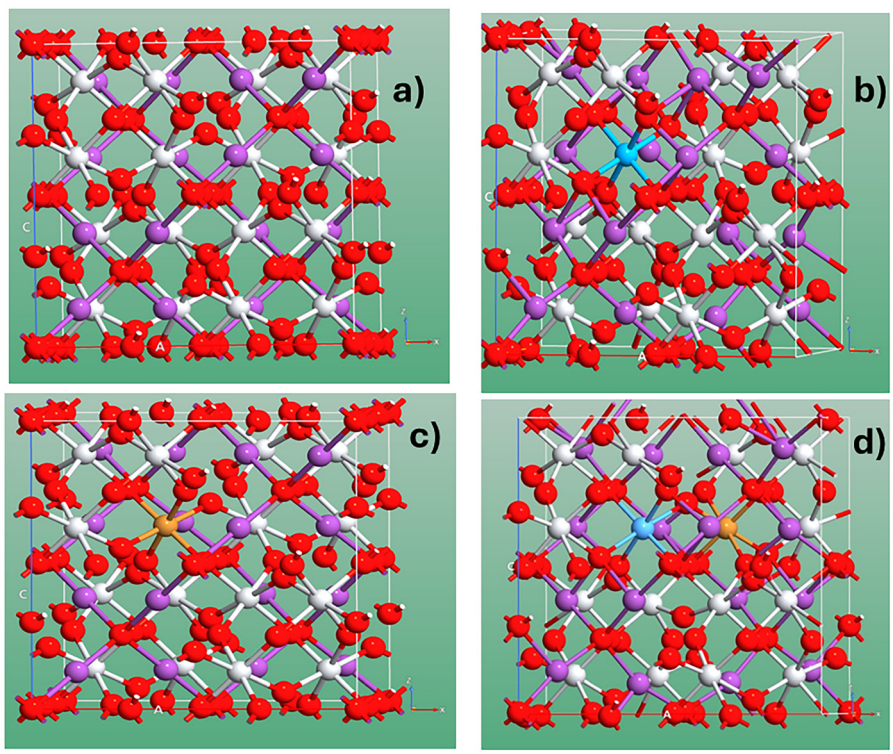

Fig. 6 (a–d) shows an optimized crystal structure used in calculations.

and energy cutoff was set at 3200 eV. We used a linear combination of atomic orbitals (LCAO) method for Bi, Ti, O, Cu & Ag atoms.

In Fig. 6(a–d), red color – oxygen; purple color – bismuth; white color – titanium; blue color – copper; golden color – silver. The electronic band structures of undoped $Bi_2Ti_2O_7$, Cu-doped, Ag-doped & co-doped $Bi_2Ti_2O_7$ are presented in Fig. 7a–d. The calculated band-gap values for the systems are 2.60, 2.28, 2.14 & 1.82 eV respectively, this underestimation is because of the well-known limitation of GGA. In the current study, we are focusing more on band-structure character and the trends in the energy gap variations through modification, rather than in calculating the absolute values. For the silver & copper doped $Bi_2Ti_2O_7$ supercell, the calculated results show an appearance of a new band near Fermi energy level, which is mainly responsible for the red shift in the experiments. Further, the shift of valence band from −1.5 eV to −0.5 eV is also observed (Fig. 7b and c). For the co-doped system (Fig. 7d), the appearance of defects states is observed above & below the Fermi energy level, which further has shifted the valence band towards more positive side shift. The trend observed in the *changes* in the energy gap corroborated well with our experimental data *i.e.* XPS and absorbance curves.

The total density of states and projected density of states (pdos) of the undoped $Bi_2Ti_2O_7$, Cu-doped, Ag-doped & co-doped $Bi_2Ti_2O_7$ are presented in Fig. 8a–d. As shown in Fig. 3a, the overlapping of Ti 3d, O 2p orbitals along with Bi 6 s and Bi 6p orbitals contributes mainly to the formation of the valence band (VB). The conduction band (CB) contributes mainly from the overlapping O 2p orbitals with unfilled Bi 6p and Ti 3d orbitals. For the Cu & Ag-doped $Bi_2Ti_2O_7$, it can be seen from Fig. 8b and c, that Cu 3d and Ag 4d localized states are formed above the valence band, and lead to the reduction of the band gap. The energy overlap of O 2p, Cu 3d & Ag 4d states can be seen, indicating hybridization, which modifies bandgap towards red shift, thereby causing widening of valence band due to O 2p states. For the co-doped $Bi_2Ti_2O_7$ (Fig. 8d), the hybridization of Ag 4d with O 2p orbitals is more pronounced, however, Cu 3d formed a discrete energy state above Fermi energy level, that may result in generation of efficient charge carriers. Our DFT based results are in well agreement with the experimental data for the improved photocatalytic activity in the co-doped $Bi_2Ti_2O_7$ system.

3.2 Morphology evaluation

Fig. 9(a–c) shows the SEM microgram images of as optimised modified mono metallic and bimetallic bismuth titanates which were carried out to evaluate their morphology and shape. The average particle size distribution of all the analytes is calculated using ImageJ software and is showcased in Table 1. From BT-Cu2 to BT-Ag2 analyte, we could observe an enhancement in average particle size and segregation of nanoparticles were also observed. In case of bimetallic analyte BTCA [Fig. 9(c)], it provided average particle size in the range of 90–129 nm and also an observation was made from mono metallic BT analytes SEM images that copper deposition made BT nanoparticles to gather together in a form of a cluster and on the other hand silver deposition promoted a net like structure with segregated nanoparticles as shown in Fig. 9(a and b). Fig. 9(d–f) demonstrated TEM microgram illustrations of BT-Cu2, BT-Ag2, and BTCA analytes which indicated that dumbbell like distinct sized particles existed in the system, size varied from BT-Cu2 with small, aggregated dumbbell shaped nanoparticles followed by BT-Ag2 with integrate large

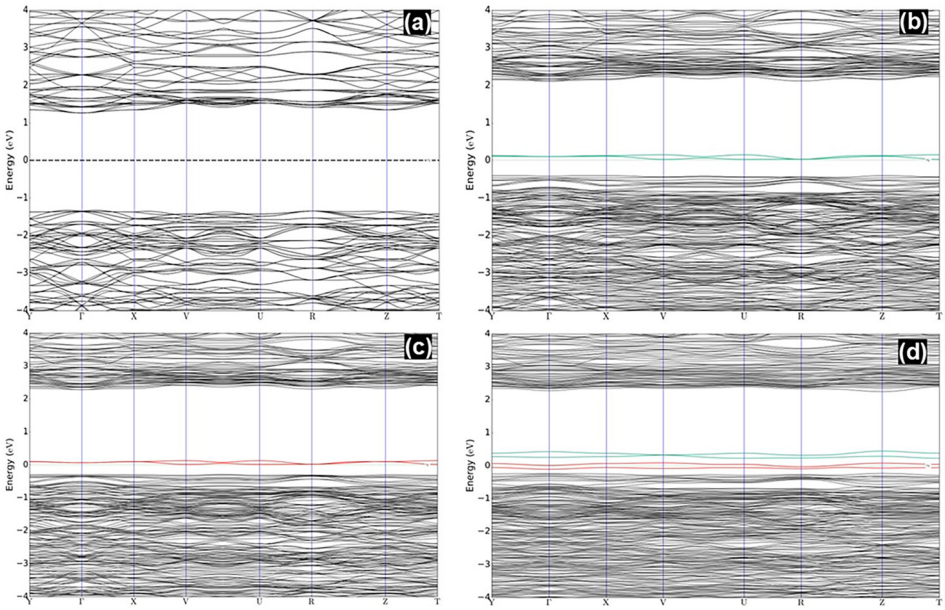

Fig. 7 (a–d) shows the electronic band structure of undoped $Bi_2Ti_2O_7$, Cu-doped (green), Ag-doped (red) & co-doped $Bi_2Ti_2O_7$.

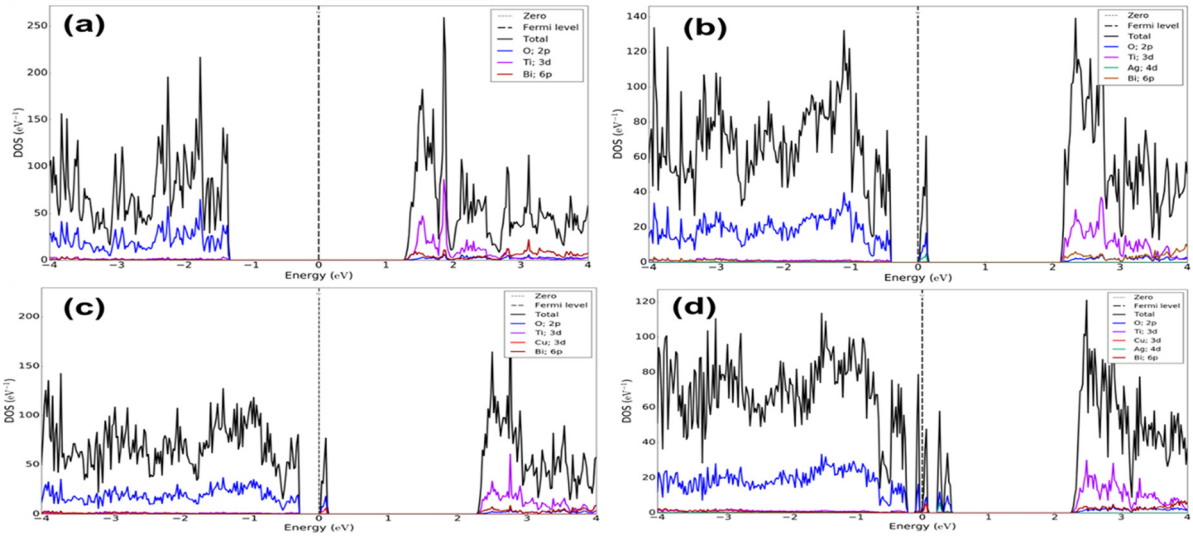

Fig. 8 (a–d) shows the total & partial density of states for undoped $Bi_2Ti_2O_7$, Cu-doped, Ag-doped & co-doped $Bi_2Ti_2O_7$.

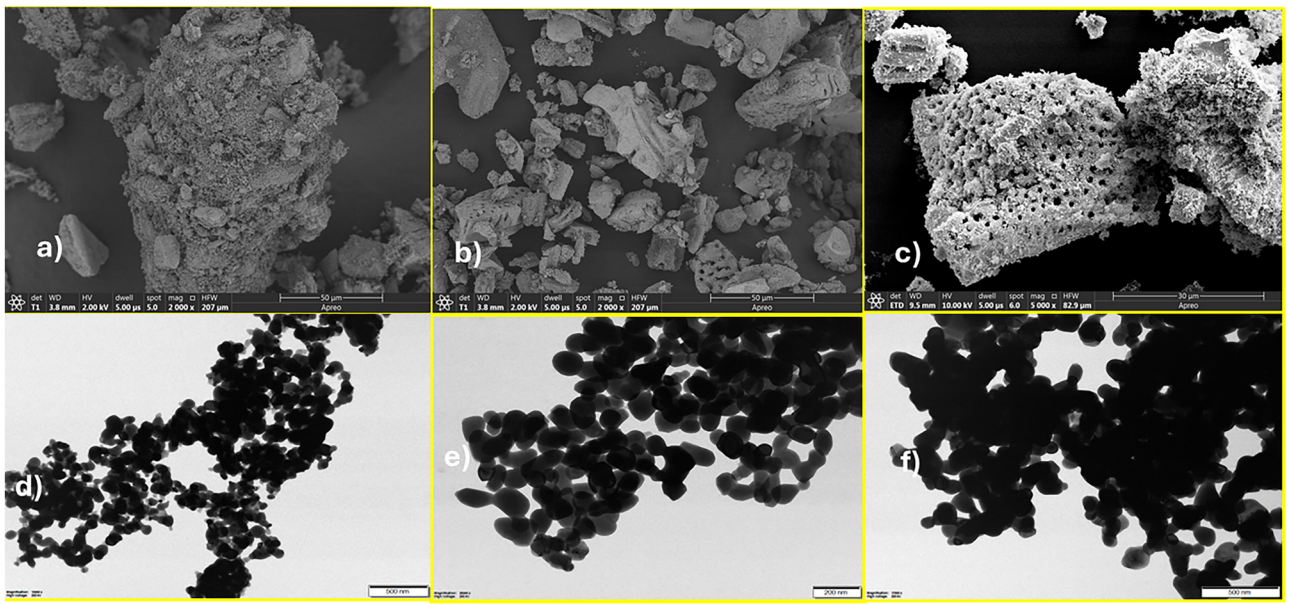

Fig. 9 SEM micrograph images of (a) BT-Cu2, (b) BT-Ag2, (c) BTCA; TEM micrograph image of (d) BT-Cu2, (e) BT-Ag2, and (f) BTCA.

dumbbell shaped crystals. The HR-TEM images, and SAED patterns of BT-Cu2, BT-Ag2, and BTCA were represented in Fig. 10 (a–f). The HR-TEM illustrations further confirmed that CuO and Ag nanoparticles was successfully dispersed on the interface of bismuth titanate. Selected Area Electron Diffraction (SAED) pattern revealed that particles of all three modified BT analytes were polycrystalline in nature. Using the ring patterns thus obtained [Fig. 10(d–f)], value of *d*-spacing was calculated for BT-Cu2, BT-Ag2, and BTCA, which well agreed with the *d*-spacing obtained from XRD analysis in the Table 1. Accordingly, the miller indices (*hkl*) values were assigned to the respective rings which was consistent with CuO secondary-phase (JCPDS card no. 48-1548),[27] and also with JCPDS file no. 04-0783 [29] for Ag nanoparticles. Exceptionally, in the case of BTCA, multiple low intensity diffraction planes in both the SAED ring pattern and the XRD of Bismuth titanate with CuO and Ag nanoparticles were discovered, demonstrating that the composite was successfully constructed with high purity of crystal lattice. The diffraction rings obtained in SAED ring pattern in Fig. 10(d) corresponds with planes {111}, {200}, {880}, {420}, {111}(CuO) for BT-Cu2 followed by the presence of crystal planes {117}, {880}, {111} (**Ag**) for BT-Ag2 and finally crystal planes of {117}, {111}(**CuO**), {880}, {200}, {111}(**Ag**), {002} (**CuO**) for BTCA. The miller indices values are well

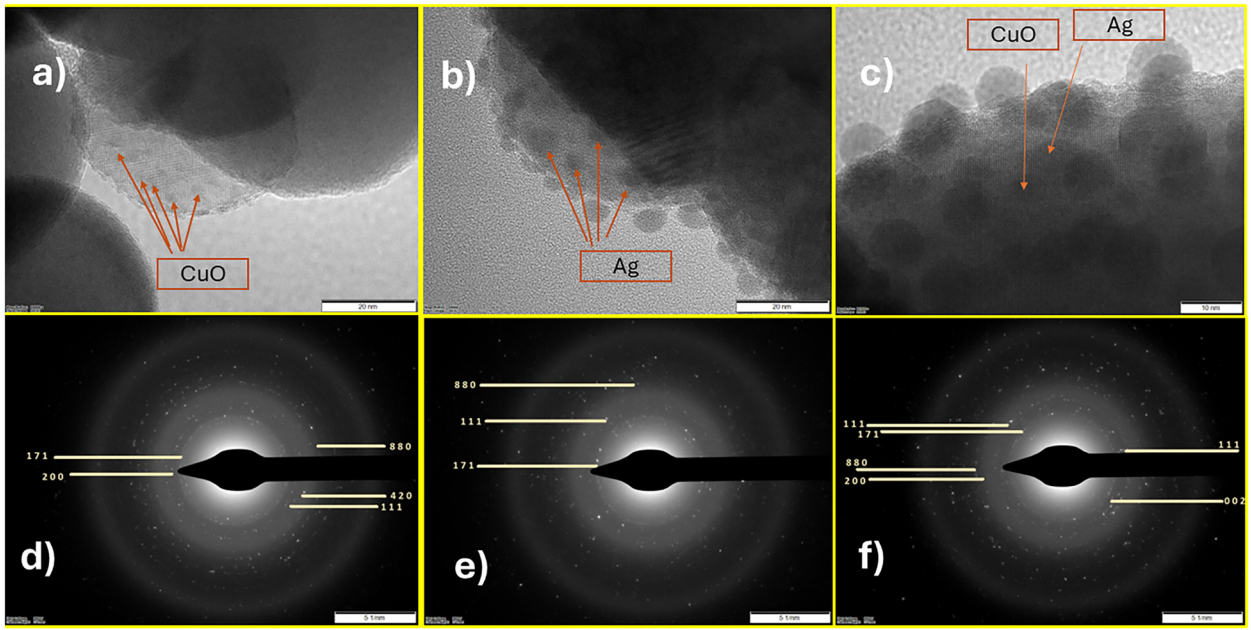

Fig. 10 HR-TEM images of (a) BT-Cu2; (b) BT-Ag2; and (c) BTCA; SAED ring pattern of (d) BT-Cu2, (e) BT-Ag2, and (f) BTCA.

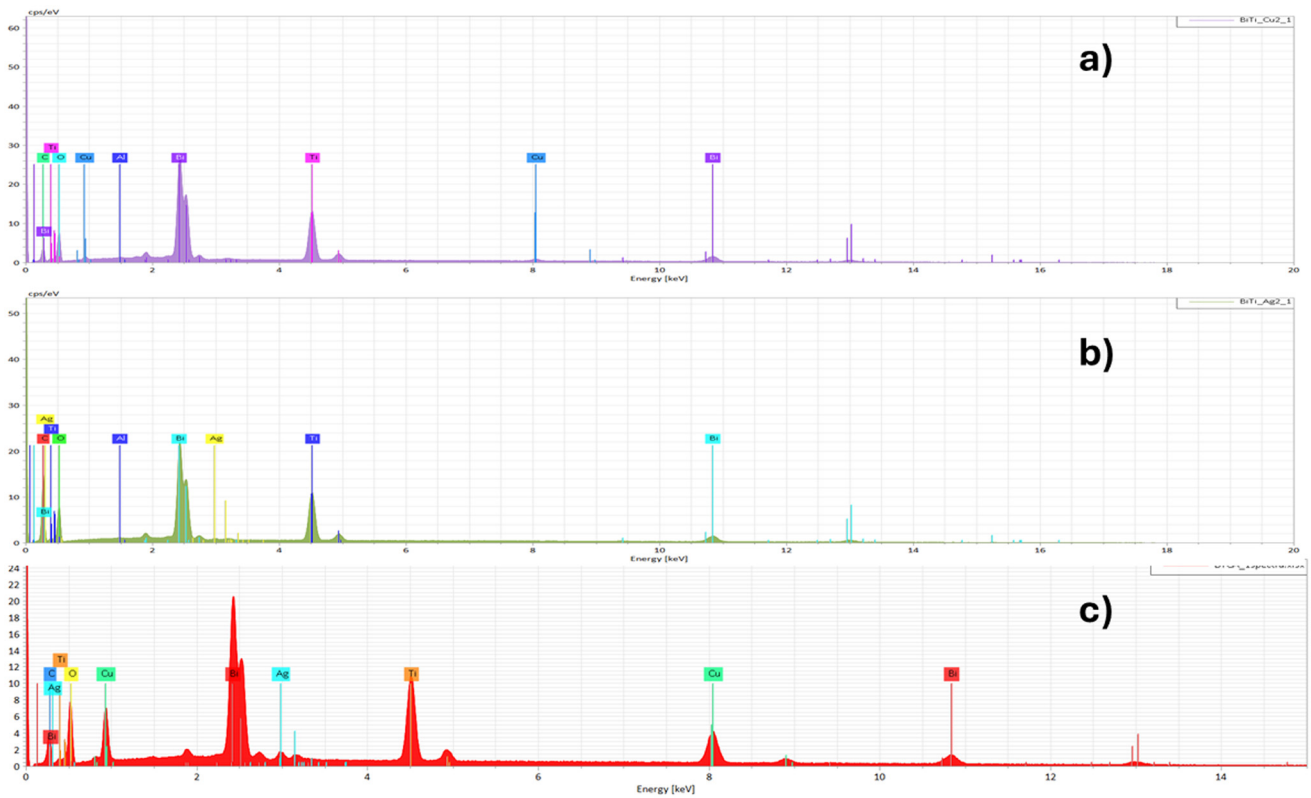

Fig. 11 EDS mapping of (a) BT-Cu2, (b) BT-Ag2, and (c) BTCA.

matched with XRD data (Fig. 2). Moreover, to confirm the presence of copper oxide composite and silver deposition at BT interface of as fabricated BT-Cu2, BT-Ag2, BTCA, EDS elemental mapping spectra [Fig. 11(a–c)] was showcased. The as obtained SEM-EDS spectra corroborated successful deposition of copper and silver on to the surface of BT thereby forming

interfacial BT nanostructure between CuO/Ag and bismuth titanate. CuO being a p-type dopant and BT being a n-type system, it was concluded to form a p–n junction among CuO and BT along with the incorporation of Ag metal at the surface of BT.

3.3 Photoelectrochemical measurements

Among the samples, BTCA and BT-Ag2 demonstrated the highest transient photocurrent responses. In contrast, BT-Cu2 showed weak photocurrent response, accompanied by a steep decline in photocurrent, indicative of significant charge carrier recombination (see Fig. 12a). As per the concentration studies, we could observe a trend that higher concentration of metals displayed the higher photocurrent response which is in accordance with their high photocatalytic efficacy. To further investigate charge carrier dynamics and transfer kinetics, electrochemical impedance spectroscopy (EIS) was performed (Fig. 12b). The EIS data aligned with the transient photocurrent results, highlighting the lowest charge transfer resistance for BTCA, followed by BT-Ag2. These two samples also delivered superior performance in CO_2 hydrogenation and pollutant degradation.

3.4 Photocatalytic degradation analysis and mechanism

The adsorption–desorption equilibrium, and photocatalytic efficacy of as fabricated BT-Cu2, BT-Ag2, and BTCA, were analysed *via* photodegradation of Bisphenol-A (BPA) (20 mg L^{-1}), under visible light irradiation as shown in Fig. 13a. Pristine BT was used as a basis to better emphasize and evaluate the role of copper oxide and silver nanoparticle in enhancing the photocatalytic degradation efficacy by modified BT analytes. In the absence of the photocatalyst, the concentration BPA remained constant over time [Fig. 13(a)]. The photocatalytic pathway is primarily linked with the surface of the photocatalyst that is exposed for adsorption of pollutants, which plays an important role in the photocatalytic disintegration of contaminants. The adsorption parameters of the as-fabricated analytes were hypothesised by establishing adsorption–desorption equilibrium *via* vigorous stirring in the absence of light. The investigation found that the adsorption–desorption equilibrium for BPA was established within 60 min of vigorous stirring in dark environment, adsorption reading was taken every 15 min and constant value was obtained at 60 min which depicted the occurrence of adsorption–desorption equilibrium. Afterwards the photocatalytic degradation of BPA using as-fabricated analytes under visible light irradiation were represented in Fig. 13a. From photocatalytic degradation experiment, in case of bimetallic bismuth titanate 'BTCA', highest degradation for BPA (80%) was reflected as compared to monometallic doped bismuth titanate samples at two distinct concentrations 'BT-Cu1, BT-Cu2, BT-Ag1, and BT-Ag2'. Higher concentration of copper and silver was responsible for higher degradation efficacy. The degradation results are in accordance with photoelectrochemical studies emphasizing least recombination centres among photogenerated charges in BTCA followed by mono metallic doped BT samples. The least recombination rate in BTCA demonstrated the presence of more active sites for degradation as compared to mono metal doped and pristine BT. The photocatalytic degradation of BPA by the as-fabricated pristine and modified BT analytes followed the pseudo-first-order kinetics model illustrated in Fig. 13b, respectively. The rate constants and regression squared values are displayed in Table 2 which summarises the calculated degradation rate constants for as-fabricated materials, as well as their photocatalytic activities. Moreover, the effect of pH was also studied for the photocatalytic degradation of BPA. The pH of the solution not only affects the conversion of ROS (reactive oxygen species) and identification of the oxidizing species and surface charge properties of the photocatalysts, but also modifies the charges of pollutants and photocatalysts, which further provides distinct degradation efficacies. As optimised BTCA analyte was checked for the photodegradation of 20 mg L^{-1} concentration of BPA with final pH values at acidic (2), neutral (7), and basic (11). In case of BPA, it was observed that the final pH of the slurry containing BTCA catalyst and BPA, was neutral and provided remarkable efficiency of 80% degradation. Whereas the degradation efficiency of BPA at keeping the final pH of the slurry at basic (12), was decreased

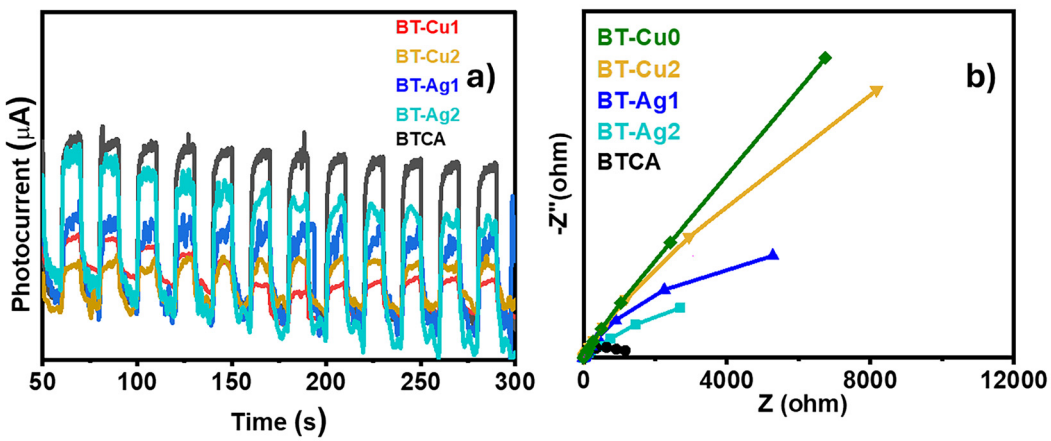

Fig. 12 Photoelectrochemical analysis of all modified BT analytes (a) Transient current response; (b) EIS Nyquist plot.

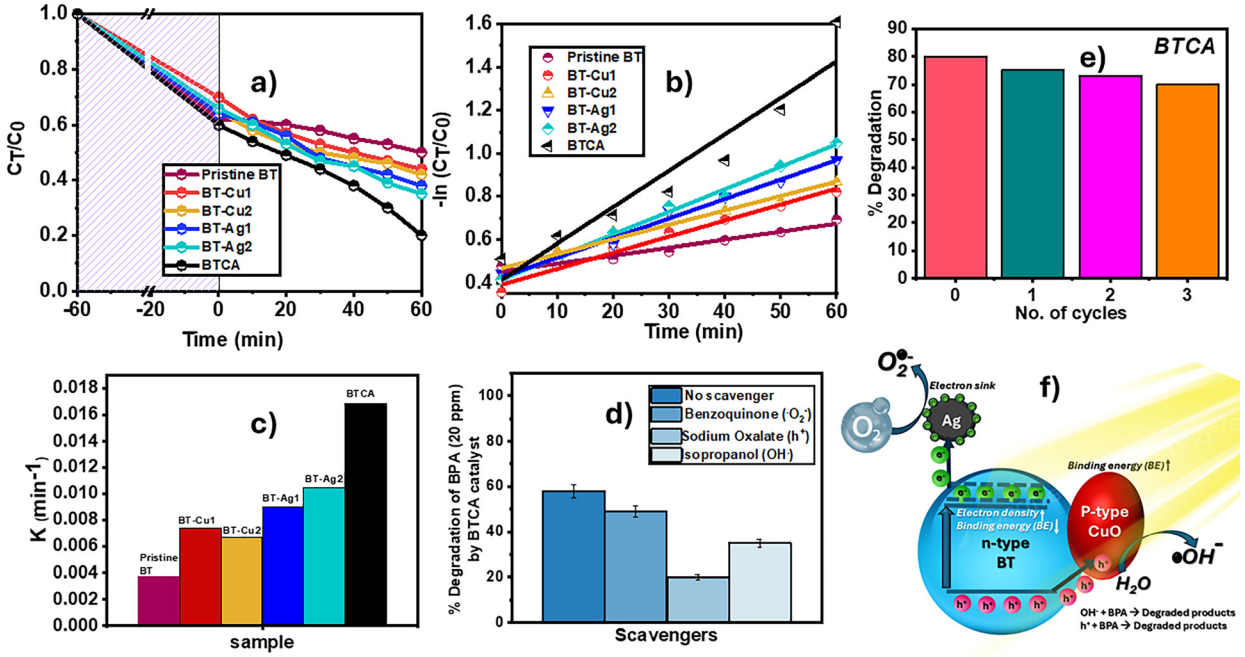

Fig. 13 Photodegradation of (a) BPA, by Pristine BT and modified BT, (b and c) kinetic linear simulation curves and rate constant values of BPA degradation over the samples, (d) radical trapping experiment on BPA degradation over BTCA analyte. (e) Recyclability studies, (f) proposed charge transfer and photodegradation mechanism of as optimised BTCA catalyst.

Table 2 Depicts the comparison among pristine and modified bismuth titanate nanostructures and their synthesis, pollutant (name and concentration), light irradiation time, degradation percentage, rate constant, regression squared value

Photocatalyst	Pollutant name	Concentration of pollutant (mg L^{-1})	Stirring time in dark (hours)	Adsorption % (approximately)	Visible light irradiation time (min)	Degradation percentage (approximately)	Rate constant	Regression squared value (R^2)
Pristine BT	BPA	20	1	38%	60	50%	0.00368	0.95894
BT-Cu1	BPA	20	1	30%	60	56%	0.00742	0.98332
BT-Cu2	BPA	20	1	35%	60	58%	0.00669	0.97015
BT-Ag1	BPA	20	1	36%	60	62%	0.00903	0.98618
BT-Ag2	BPA	20	1	34%	60	65%	0.01046	0.993
BTCA	BPA	20	1	40%	60	80%	0.01688	0.91625

substantially, due to the occurrence of repulsive forces among the negative charge at BTCA and OH^- ions on BPA slurry at basic pH after addition of NaOH. At neutral pH (7) maximum number of active sites and optimal hydroxyl free radicals were present due to decrease in the repulsive forces among catalyst and the pollutant solution. Finally, degradation extent of BPA was also checked at acidic pH value (2), which provided further lesser degradation, which might be attributed to photocatalyst agglomeration in the final solution, which in turn reduced the exposed surface of the photocatalyst for photon absorption while increasing electron–hole recombination.

The synergistic compositing of p-type CuO and Ag nanoparticles in n-type into BT, considerably enhanced the photocatalytic disintegration of BPA as mentioned in the proposed mechanism in Fig. 13f, within this heterostructure, CuO having a narrow band gap serves as a hole acceptor, while the electron sinks are Ag nanoparticles. XPS also demonstrated a significant binding energy shift in Cu 2p, and Ag 3d orbitals towards higher values from the pristine BT, indicating electron deposition at these positions. Simultaneously, the downward binding energy shift in Bi 4f indicates electron loss from the Bi–O lattice, representing an internal transfer of electrons from the BT matrix to the CuO and Ag phases. Under light illumination, photogenerated electrons in the conduction band (CB) of BT are transferred quickly to Ag, whereas holes in the valence band (VB) are efficiently scavenged by CuO. The bidirectional charge migration significantly inhibits electron–hole recombination, further evidenced by photoelectrochemical (PEC) measurement of increased photocurrent. The electrons transferred on Ag enable O_2 reduction to reactive oxygen species ($^{\bullet}O_2^-$), whereas holes stored in CuO enable oxidation

reactions, including the formation of hydroxyl radical ($^{\bullet}OH$). The generated H^+ and $^{\bullet}OH^-$ interacted with BPA that disintegrated it into small molecules. The excited electrons present in CB reacted with atmospheric O_2 and produced superoxide radical ($^{\bullet}O_2^-$). The amount of pollutant, adsorbed on the surface of as-fabricated BTCA, directly affected the degradation percentage and rate of the degradation of pollutant.

3.4.1 Scavenging study. During the photocatalytic process, reactive radical species [holes (h^+), hydroxyl radicals ($^{\bullet}OH$), and superoxide radicals (O_2^-)] are generated after photon absorption. Therefore, to elucidate proper mechanism of photocatalytic degradation, the trapping experiments were conducted using the as optimized BTCA sample combination to investigate the active species responsible for the degradation BPA. Sodium oxalate, isopropanol, and benzoquinone were used as scavengers for holes (h^+), hydroxyl radicals ($^{\bullet}OH$), and superoxide radicals (O_2^-), respectively. As shown in Fig. 13d, a noticeable reduction in photocatalytic activity was observed, with a significant decrease in the degradation of pollutant by trapping holes and superoxide radical species. Similarly, the photodegradation efficiency of BPA (Fig. 13d) was significantly reduced with the introduction of sodium oxalate, suggesting that holes were the primary active species in the photo-oxidation process. Moreover, Fig. 13d also indicated a proximal decrease in degradation % of BPA by adding benzoquinone promoting that superoxide radicals were also involved as the key active species in the photodegradation of BPA.

3.4.2 Recyclability test. To evaluate the stability and repeatability of the optimized BTCA analyte, three consecutive experimental cycles were performed for the photocatalytic degradation of BPA solutions (Fig. 13e). After each cycle, as optimised BTCA analyte depicted 2–3% decline in the photocatalytic efficacy of BPA degradation. This showed that the BTCA photocatalyst exhibited excellent stability, maintaining its photocatalytic performance with minimal decline under visible light irradiation.

3.5 Photocatalytic CO_2 reduction and its mechanism

The photocatalytic CO_2 hydrogenation efficiency including CO_2 conversion %, estimated production rates, selectivity % values of as- fabricated pristine and modified BT analytes (Pristine BT, BT-Cu1, BT-Cu2, BT-Ag1, BT-Ag2, and BTCA), was depicted in Table 3. In the absence of photocatalysts, no conversion occurred. Highest CO_2 conversion percentage was seen in BTCA analyte which is bimetal doped bismuth titanate. In BTCA, due to the deposition of Ag nanoparticles and junction with CuO, reduced recombination thereby a greater number of electrons were readily present in these analytes with high transportation rates. Furthermore, if we differentiate among all modified BT-analytes, we could observe that silver, and bimetal modified analytes have shown remarkable CO_2 photoconversion efficiency as well as an increase in production concentration for CH_4. Moreover, after modifying pristine BT with copper and silver for all analytes, selectivity towards methane was also enhanced which was the prior objective for promoting more interfacial electron transfer by addition of metal and to reduce the recombination rate among photogenerated charge carriers. In case of BT-Cu2 analyte, photogenerated electrons from the pristine BT collectively enhanced the electron density. Also, upon irradiation, highly dispersed Cu^{2+} changed to Cu^+ at the surface which helped to bind the *in situ* generated CO which further underwent C–C coupling. This transition in oxidation state helped to attain the higher selectivity towards CH_4 as compared to pristine BT. In case of BT-Ag2, silver metal in its Ag 3d state and also in its oxide form, created an impurity band of BT, thus shifting the absorption edge to the visible region thereby promoting more separation among photogenerated charge carriers. Most probably based of the Fermi level of BT analyte, we could promote a hypothesis that Ag metal has formed a metal cluster and provided abundant electrons to pristine BT which predominately enhanced the CO_2 conversion extent, whereas both the metals copper and silver worked wonder as a combined dopant in the lattice of pristine BT, it provided continuous charge transfer in BTCA analyte, which further showcased highest conversion extent among mono metallic doped BT analytes and pristine BT analyte. Fig. 14(b) depicts the conversion of CO_2 from 0 min to 189 min. As per Fig. 14(a), we could observe that CO selectivity was 90–97%, whereas CH_4 selectivity was 2–9%. With the increasing conversion %, CH_4 selectivity % also enhanced. This possibly depicts that methane production occurs requires more charge carriers for this process than for CO_2 to CO conversion. In case of BTCA offered the highest conversion % with enhanced CH_4 selectivity followed by monometallic doped BT-Cu and BT-Ag analytes.[26,28,29,36,37] During light irradiation, photogenerated electrons are transported to Ag sites (electron sinks) while

Table 3 Depicting the CO_2 conversion % and production rates of C1 products in nmol g^{-1} h^{-1} as well as their selectivity %

		CO			CH_4		
Sample	CO_2 conversion (%)	Amount of CO produced (nmol in 3.15 h)	CO production rate (nmol g^{-1} h^{-1})	Selectivity %	Amount of CH_4 produced (nmol in 3.15 h)	CH_4 production rate (nmol g^{-1} h^{-1})	Selectivity (%)
Pristine BT	25.5	907.21	1530	90.54626	94.72	138	9.45374
BT-Cu1	26.7	967.37	1467.6	90.77196	98.34	41.45	9.228043
BT-Cu2	**27.5**	**984.18**	**1375.242**	**88.7998**	**124.13**	**152.322**	**11.2002**
BT-Ag1	33.8	1396.08	1714.8	93.46819	97.56	144.237	6.531806
BT-Ag2	**34.5**	1431.08	1923.705	92.90621	109.27	161.544	7.09379
BTCA	**39.1**	**1719.23**	**2391.06**	**91.79539**	**153.66**	**73.4**	**8.20461**

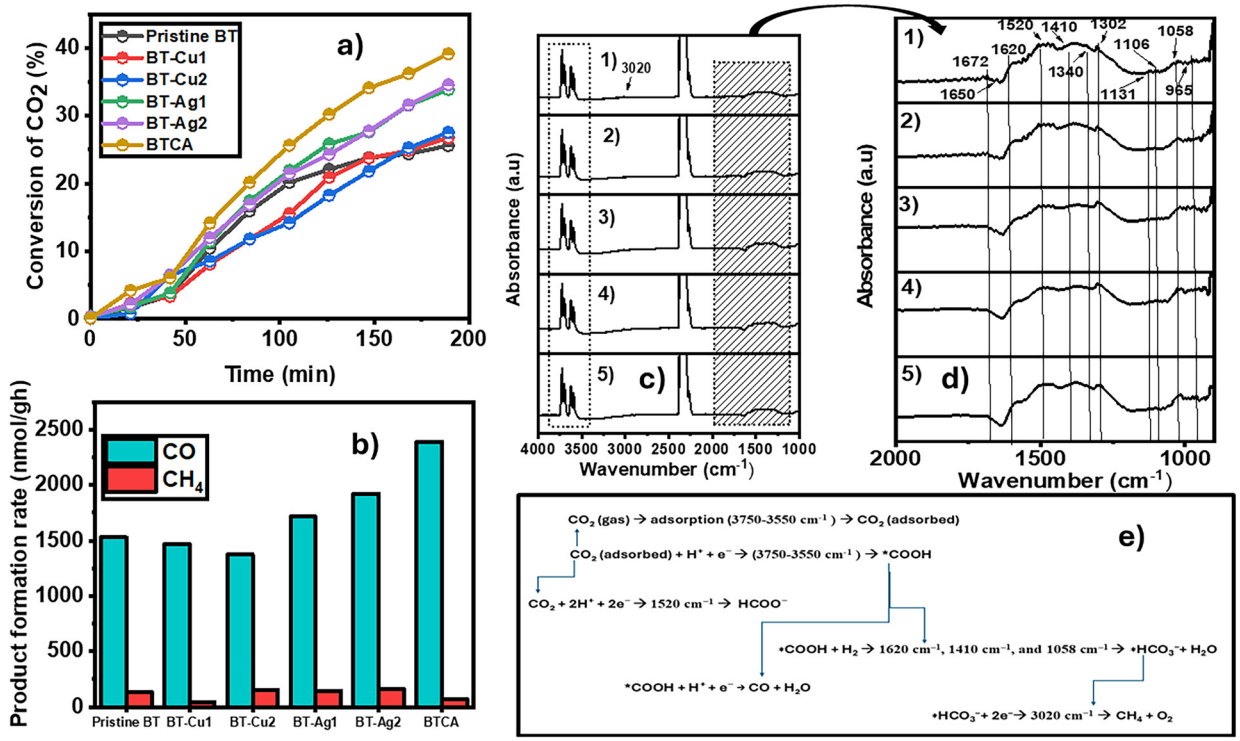

Fig. 14 (a) Conversion % of CO_2, (b) product formation rate (CO and CH_4), (c and d) DRIFTS spectra of as optimised BTCA sample. The numbers in the figure represent the following: (1) Reference measurement in H_2 atmosphere, (2) at room temperature, (3) at room temperature + under UV exposure for 10 min, (4) at room temperature + under UV exposure for 20 min, and (5) without UV exposure; (e) reaction scheme for CO_2 adsorption and hydrogenation to CO and CH_4.

holes migrate to Cu sites (hole acceptors), allowing charge separation. In order to better understand the catalytic CO_2 photoreduction reaction pathway, *in situ* DRIFTS characterisation of as optimised BTCA was carried out and properly stated in the reaction scheme as demonstrated in Fig. 14e. Two prominent twin-bands at 3750–3550 cm^{-1} correspond to combined tones gas and adsorbed CO_2 molecules in BTCA. Bands seen at 1672 cm^{-1} and 1340 cm^{-1} can be attributed to carboxylic species (*COOH), which are one of the major intermediates during the photocatalytic reduction of CO_2 to CO and CH_4. The bands at 1620 cm^{-1}, 1410 cm^{-1}, and 1058 cm^{-1} are adsorbed bicarbonate species.[38] Bands at 1650 and 1440 cm^{-1} correspond to the O–C–O stretch of bicarbonates. A band at 3020 cm^{-1} corresponds to CH_4, C–H stretch vibrations, while a peak at 1520 cm^{-1} indicates formate species (HCOO).[39]

4 Conclusion and future perspectives

Depositing copper oxide (CuO) as a p-type material and silver (Ag) metal onto the interfacial bismuth titanate (BT) n-type heterostructure structure resulted in significant enhancements in photocatalytic performance and CO_2 photoreduction efficiency compared to pristine BT. Notably, bimetallic modified BT "BTCA" provided the superior CO_2 conversion rate of 39.1%, with carbon monoxide (CO) being the primary product, while methane (CH_4) was also produced, albeit in smaller quantities. The study discovered a trade-off: higher rates of CO_2 conversion resulted in decreased selectivity for methane (CH_4), underlining the importance of electron transport in the photoreduction process. Improvements in photocatalytic CO_2 reduction are attributed to enhanced interfacial charge transfer, increased surface area, band gap modification. In contrast to our work with undoped bismuth titanate (Pristine BT), metal modification significantly boosts its performance, making it a promising material for sustainable CO_2 reduction. The improved methane selectivity observed with copper-doped BT (BT-Cu2) is linked to a light-induced change in the copper's oxidation state at the surface. The resulting Cu^{1+} species plays a crucial role in binding CO molecules and enabling carbon–carbon coupling, a key step in methane formation. This mechanism explains the enhanced performance compared to pristine BT. In silver-doped bismuth titanate (BT-Ag2), the presence of silver, both as metallic Ag (Ag 3d state) (confirmed by XRD), creates an "impurity band" within the structure of the BT. This impurity band shifts the material's light absorption range towards the visible spectrum, leading to more efficient separation of photogenerated electrons and holes. We hypothesize, based on the Fermi level of BT, that the silver forms metallic clusters that donate a large number of electrons to the surface of the pristine BT, signifi-

cantly enhancing the conversion of CO_2. DFT calculations revealed that for the Cu & Ag-modified BT that Cu 3d and Ag 4d localized states are formed above the valence band and led to the reduction of the band gap. For the co-doped BT, the hybridization of Ag 4d with O 2p orbitals is more pronounced, however, Cu 3d formed a discrete energy state above Fermi energy level, that may result in generation of efficient charge carriers. DFT based results were in well agreement with the experimental data for the improved photocatalytic activity in the co-doped $Bi_2Ti_2O_7$ system. Copper and silver, when used together as dopants with the BT lattice, demonstrated a remarkable synergistic effect. Furthermore, Photocatalytic degradation experiments also revealed that bimetallic BTCA was the most effective in BPA (80%) compared to Pristine BT and monometallic BT-Cu2, BT-Ag2. Importantly, the degradation efficiencies correlated well with PEC measurements, showing that BTCA exhibited the lowest photogenerated charge recombination rate, followed by BT-Ag2 and BT-Cu2. The reduced recombination in BTCA indicates a greater number of active sites than the pristine BT, leading to enhanced degradation. Also, in case of CO_2 hydrogenation, BTCA provided a prominent enhancement in conversion %, and BT-Cu2 provided huge selectivity towards methane which is correlated with the high production and transfer of electrons based on experimental and first principal analysis. Additionally, to further confirm the mechanism for photocatalytic CO_2 hydrogenation, DRIFT spectra was carried out and we observed that carboxyl (*COOH) and formate (*HCOO–) were the key intermediate in the formation of CO and CH_4 during the reaction mechanism for bimetallic doped BT (BTCA). Future research should focus on optimizing dopant combinations and concentrations to further improve the performance of BT-based catalysts for energy and environmental applications.

Author contributions

Isha Arora, Seema Garg, Andras Sapi: conceptualization, methodology; Mohit Yadav, Ajay, Zoltán Kónya: software, data curation; Isha Arora: data curation, visualization, investigation, writing – original draft preparation; Seema Garg, Andras Sapi, Pravin Popinand Ingole, Amrish Chandra: visualization, investigation, supervision, software, validation; Isha Arora, Seema Garg: writing – reviewing and editing.

Conflicts of interest

There are no conflicts to declare.

Data availability

All the data supporting this article have been included in the main article.

Acknowledgements

I would like to express my sincere gratitude to the Amity Institute of Applied Sciences for providing invaluable support and resources during the course of this research. My heartfelt thanks go to Department of Chemistry, IIT Delhi for their inspiring guidance and the use of their facilities. I am deeply grateful to University of Szeged for their encouragement constant guidance and the utilisation of their hightech facilities for collaboration throughout this project.

The author (Sumant Upadhyay) is thankful to the Science and Engineering Research Board, Govt of India (SERB) under the TARE scheme for financial support (TAR/2021/000100).

We as gratefully acknowledges the support of FK 143583 and ZK is grateful for K_21 138714 project from the source of the National Research, Development and Innovation Fund. Project no. RRF-2.3.1-21-2022-00009, titled National Laboratory for Renewable Energy has been implemented with the support provided by the Recovery and Resilience Facility of the European Union within the framework of Programme Széchenyi Plan Plus.

I would also like to express my sincere gratitude to the following individuals for their invaluable contributions to this research. Special thanks to Imre Szenti for providing the SEM images, Akos Szamosvölgyi for sharing the XPS data, and Dr Harshita Chawla for her assistance with the CO_2 photoreduction calculations. I also appreciate Fanni Czirok for providing the BET graphs and DRIFT spectra. All of these individuals are from the University of Szeged, and their expertise and support have been crucial to the success of this work.

References

1 M. Yadav, S. Garg, A. Chandra and K. Hernadi, Immobilization of green BiOX (X= Cl, Br and I) photocatalysts on ceramic fibers for enhanced photocatalytic degradation of recalcitrant organic pollutants and efficient regeneration process, *Ceram. Int.*, 2019, **45**, 17715–17722, DOI: **10.1016/j.ceramint.2019.05.340**.

2 S. Singh, A. Chaki, D. P. Chand, A. Raghuwanshi, P. K. Singh and H. Mahalingham, A novel polystyrene-supported titanium dioxide photocatalyst for degradation of methyl orange and methylene blue dyes under UV irradiation, *J. Chem.*, 2014, **28**, 9–13, DOI: **10.3329/jce.v28i1.18103**.

3 Q. Wang, J. Hui, J. Li, Y. Cai, S. Yin, F. Wang and B. Su, Photodegradation of methyl orange with PANI-smodified BiOCl photocatalyst under visible light irradiation, *Appl. Surf. Sci.*, 2013, **283**, 577–583, DOI: **10.1016/j.apsusc.2013.06.149**.

4 S. Kader, M. R. Al-Mamun, M. B. K. Suhan, S. B. Shuchi and M. S. Islam, Enhanced photodegradation of methyl orange dye under UV irradiation using MoO3 and Ag doped TiO2 photocatalysts, *Environ. Technol. Innovation*, 2022, **27**, 102476, DOI: **10.1016/j.eti.2022.102476**.

5 D. P. Subagio, M. Srinivasan, M. Lim and T. T. Lim, Photocatalytic degradation of bisphenol-A by nitrogen-doped TiO2 hollow sphere in a vis-LED photoreactor, *Appl. Catal., B*, 2010, **95**, 414–422, DOI: **10.1016/j.apcatb.2010.01.021**.

6 Y. Kanigaridou, A. Petala, Z. Frontistis, M. Antonopoulou, M. Solakidou, I. Konstantinou, Y. Deligiannakis, D. Mantzavinos and D. I. Kondarides, Solar photocatalytic degradation of bisphenol A with CuOx/BiVO4: Insights into the unexpectedly favorable effect of bicarbonates, *Chem. Eng. J.*, 2017, **318**, 39–49, DOI: **10.1016/j.cej.2016.04.145**.

7 C. Y. Wang, Y. J. Zhang, W. K. Wang, D. N. Pei, G. X. Huang, J. J. Chen, X. Zhang and H. Q. Yu, Enhanced photocatalytic degradation of bisphenol A by Co-doped BiOCl nanosheets under visible light irradiation, *Appl. Catal., B*, 2018, **221**, 320–328, DOI: **10.1016/j.apcatb.2017.09.036**.

8 M. Pan, H. Zhang, G. Gao, L. Liu and W. Chen, Facet-dependent catalytic activity of nanosheet-assembled bismuth oxyiodide microspheres in degradation of bisphenol A, *Environ. Sci. Technol.*, 2015, **49**, 6240–6248, DOI: **10.1021/acs.est.5b00626**.

9 W. He, Y. Wei, J. Xiong, Z. Tang, W. Song, J. Liu and Z. Zhao, Insight into reaction pathways of CO2 photoreduction into CH4 over hollow microsphere Bi2MoO6-supported Au catalysts, *Chem. Eng. J.*, 2022, **433**, 133540, DOI: **10.1016/j.cej.2021.133540**.

10 N. Li, M. Liu, B. Yang, W. Shu, Q. Shen, M. Liu and J. Zhou, Enhanced Photocatalytic Performance toward CO2 Hydrogenation over Nanosized TiO2-Loaded Pd under UV Irradiation, *J. Phys. Chem. C*, 2017, **121**, 2923–2932, DOI: **10.1021/acs.jpcc.6b12683**.

11 A. Meng, B. Cheng, H. Tan, J. Fan, C. Su and J. Yu, TiO2/polydopamine S-scheme heterojunction photocatalyst with enhanced CO2-reduction selectivity, *Appl. Catal., B*, 2021, **289**, 120039, DOI: **10.1016/j.apcatb.2021.120039**.

12 Ž Kovačič, B. Likozar and M. Huš, Photocatalytic CO2Reduction: A Review of Ab Initio Mechanism, Kinetics, and Multiscale Modeling Simulations, *ACS Catal.*, 2020, **10**, 14984–15007, DOI: **10.1021/acscatal.0c02557**.

13 I. Arora, S. Garg, A. Sapi, P. P. Ingole and A. Chandra, Insights into photocatalytic CO2 reduction reaction pathway: Catalytic modification for enhanced solar fuel production, *J. Ind. Eng. Chem.*, 2024, **137**, 1–28, DOI: **10.1016/j.jiec.2024.03.011**.

14 D. Fei, Y. Peng, F. Tang, Z. Liu, R. Wang, L. Chen, X. Liu, X. Chen, M. Song and H. Hao, Simultaneous enhancement of the optical absorption, ferroelectric polarization, and photocatalytic activity by designing the Ti/Fe ratio for Bi5Ti3FeO15, *Ceram. Int.*, 2024, **50**, 12017–12027, DOI: **10.1016/j.ceramint.2024.01.104**.

15 Y. Zhao, Y. Zhang, Q. Xu, H. Gong, M. Yan, K. Feng, X. Zhou, X. Zhou and D. Zhang, Enhanced piezoelectricity and spectral absorption in Nd-doped bismuth titanate hierarchical microspheres for efficient piezo-photocatalytic H2 production and pollutant degradation, *J. Mater. Chem. A*, 2024, **12**, 1753–1763, DOI: **10.1039/d3ta06341k**.

16 X. Liu, J. Wang, F. Zhu, Y. Li, W. Tian, W. Wang, R. Guo, L. Liu and J. Shi, Surface oxygen vacancy engineering in weak Bi-O bonded ferroelectric bismuth sodium titanate for boosting the photocatalytic CO2 reduction reaction, *J. Mater. Chem. A*, 2024, **12**, 9661–9671, DOI: **10.1039/d4ta01030b**.

17 S. Li, J. Liu, T. Guo, W. Dong, K. Bi and Y. Luo, Piezoelectricity and flexoelectricity of sodium bismuth titanate-based ceramics, *Ceram. Int.*, 2020, **46**, 2049–2054, DOI: **10.1016/j.ceramint.2019.09.184**.

18 A. S. Anokhin, N. V. Lyanguzov, S. B. Roshal', Y. I. Yuzyuk and W. Wang, Raman spectra of polycrystalline bismuth titanate nanotubes, *Phys. Solid State*, 2011, **53**, 1867–1871, DOI: **10.1134/S1063783411090034**.

19 L. Z. Pei, H. D. Liu, N. Lin and H. Y. Yu, Bismuth titanate nanorods and their visible light photocatalytic properties, *J. Alloys Compd.*, 2015, **622**, 254–261, DOI: **10.1016/j.jallcom.2014.10.008**.

20 L. Z. Pei, H. D. Liu, N. Lin and H. Y. Yu, Bismuth titanate nanorods and their visible light photocatalytic properties, *J. Alloys Compd.*, 2015, **622**, 254–261, DOI: **10.1016/j.jallcom.2014.10.008**.

21 L. Kong, H. Chen, W. Hua, S. Zhang and J. Chen, Mesoporous bismuth titanate with visible-light photocatalytic activity, *Chem. Commun.*, 2008, 4977–4979, DOI: **10.1039/b808911f**.

22 A. R. Noviyanti, D. R. Eddy and M. D. Permana, Risdiana, Heterophase of Bismuth Titanate as a Photocatalyst for Rhodamine B Degradation, *Trends Sci.*, 2023, **20**, 6147, DOI: **10.48048/tis.2023.6147**.

23 J. Chen, W. Mei, C. Liu, C. Hu, Q. Huang, N. Chen, J. Chen, R. Zhang and W. Hou, Carbon-modified bismuth titanate with an enhanced photocatalytic activity under nature sunlight, *Mater. Lett.*, 2016, **172**, 184–187, DOI: **10.1016/j.matlet.2016.03.002**.

24 S. Murugesan, M. N. Huda, Y. Yan, M. M. Al-Jassim and V. Subramanian, Band-engineered bismuth titanate pyrochlores for visible light photocatalysis, *J. Phys. Chem. C*, 2010, **114**, 10598–10605, DOI: **10.1021/jp906252r**.

25 A. A. Correya, A. Nadeer, V. P. N. Nampoori and A. Mujeeb, The Effect of Polyethylene Glycol on the Formation of Bismuth Titanate Nanosheets and Its Effect on Optical Characteristics, *J. Cluster Sci.*, 2023, **34**, 1437–1444, DOI: **10.1007/s10876-022-02290-x**.

26 S. Ali, A. Razzaq, H. Kim and S. Il In, Activity, selectivity, and stability of earth-abundant CuO/Cu2O/Cu0-based photocatalysts toward CO2 reduction, *Chem. Eng. J.*, 2022, **429**, 131579, DOI: **10.1016/j.cej.2021.131579**.

27 K. Wu and C. Zhang, Facile synthesis and ppb-level H_2S sensing performance of hierarchical CuO microflowers assembled with nano-spindles, *J. Mater. Sci.: Mater. Electron.*, 2020, **31**, 7937–7945, DOI: **10.1007/s10854-020-03332-8**.

28 K. Kočí, K. Matějů, L. Obalová, S. Krejčíková, Z. Lacný, D. Plachá, L. Čapek, A. Hospodková and O. Šolcová, Effect of silver doping on the TiO2 for photocatalytic reduction of CO2, *Appl. Catal., B*, 2010, **96**, 239–244, DOI: **10.1016/j.apcatb.2010.02.030**.

29 Y. Yang, N. Liu, S. Qiao, R. Liu, H. Huang and Y. Liu, Silver modified carbon quantum dots for solvent-free selective oxidation of cyclohexane, *New J. Chem.*, 2015, **39**, 2815–2821, DOI: **10.1039/c4nj02256d**.

30 A. S. Malik, H. Bali, F. Czirok, Á. Szamosvölgyi, G. Halasi, A. Efremova, B. Šmíd, A. Sápi, Á. Kukovecz and Z. Kónya, Turning CO2 to CH4 and CO over CeO_2 and MCF-17 supported Pt, Ru and Rh nanoclusters – Influence of nanostructure morphology, supporting materials and operating conditions, *Fuel*, 2022, **32**, 124994, DOI: **10.1016/j.fuel.2022.124994**.

31 Y. Wang, W. Duan, B. Liu, X. Chen, F. Yang and J. Guo, The effects of doping copper and mesoporous structure on photocatalytic properties of TiO, *J. Nanomater.*, 2014, 178152, DOI: **10.1155/2014/178152**.

32 M. P. Rao, J. J. Wu, A. M. Asiri, S. Anandan and M. Ashokkumar, Photocatalytic properties of hierarchical CuO nanosheets synthesized by a solution phase method, *J. Environ. Sci.*, 2018, **69**, 115–124, DOI: **10.1016/j.jes.2017.05.005**.

33 M. M. Zahornyi, N. I. Tyschenko, T. F. Lobunets, O. F. Kolomys, V. V. Strelchuk, K. S. Naumenko, L. O. Biliavska, S. D. Zahorodnia, O. M. Lavrynenko and A. I. Ievtushenko, The Ag Influence on the Surface States of TiO2, Optical Activity and Its Cytotoxicity, *J. Nano- Electron. Phys.*, 2021, **13**, 06009, DOI: **10.21272/JNEP.13(6).06009**.

34 P. E. Blochl, Projector augmented-wave method, *Phys. Rev. B*, 1994, **50**, 17953, DOI: **10.1103/PhysRevB.50.17953**.

35 G. Kresse and D. Joubert, From ultrasoft pseudopotentials to the projector augmented-wave method, *Phys. Rev. B*, 1999, **59**, DOI: **10.1103/PhysRevB.59.1758**.

36 P. Bamola, C. Dwivedi, A. Gautam, M. Sharma, S. Tripathy, A. Mishra and H. Sharma, Strain-induced bimetallic nanoparticles-TiO2 nanohybrids for harvesting light energy, *Appl. Surf. Sci.*, 2020, **511**, 145416, DOI: **10.1016/j.apsusc.2020.145416**.

37 W. J. Dong, J. W. Lim, D. M. Hong, J. Kim, J. Y. Park, W. S. Cho, S. Baek and J. L. Lee, Grain Boundary Engineering of Cu-Ag Thin-Film Catalysts for Selective (Photo)Electrochemical CO2Reduction to CO and CH4, *ACS Appl. Mater. Interfaces*, 2021, **13**, 18905–18913, DOI: **10.1021/acsami.1c03735**.

38 M. Yadav, T. Gyulavári, J. Kiss, K. B. Ábrahámné, A. Efremova, Á. Szamosvölgyi, Z. Pap, A. Sápi, Á. Kukovecz and Z. Kónya, Noble metal nanoparticles and nanodiamond modified strontium titanate photocatalysts for room temperature CO production from direct hydrogenation of CO2, *J. CO_2 Util.*, 2023, **78**, 102621, DOI: **10.1016/j.jcou.2023.102621**.

39 L. Proaño, E. Tello, M. A. Arellano-Trevino, S. Wang, R. J. Farrauto and M. Cobo, *In situ* DRIFTS study of two-step CO 2 capture and catalytic methanation over Ru,"Na 2 O"/Al 2 O 3 Dual Functional Material, *Appl. Surf. Sci.*, 2019, **479**, 25–30, DOI: **10.1016/j.apsusc.2019.01.281**.